

# SpectralDiff: Hyperspectral Image Classification with Spectral-Spatial Diffusion Models

Ning Chen, Jun Yue, Leyuan Fang, *Senior Member, IEEE*, and Shaobo Xia

**Abstract**—Hyperspectral image (HSI) classification is an important topic in the field of remote sensing, and has a wide range of applications in Earth science. HSIs contain hundreds of continuous bands, which are characterized by high dimension and high correlation between adjacent bands. The high dimension and redundancy of HSI data bring great difficulties to HSI classification. In recent years, a large number of HSI feature extraction and classification methods based on deep learning have been proposed. However, their ability to model the global relationships among samples in both spatial and spectral domains is still limited. In order to solve this problem, an HSI classification method with spectral-spatial diffusion models is proposed. The proposed method realizes the reconstruction of spectral-spatial distribution of the training samples with the forward and reverse spectral-spatial diffusion process, thus modeling the global spatial-spectral relationship between samples. Then, we use the spectral-spatial denoising network of the reverse process to extract the unsupervised diffusion features. Features extracted by the spectral-spatial diffusion models can achieve cross-sample perception from the reconstructed distribution of the training samples, thus obtaining better classification performance. Experiments on three public HSI datasets show that the proposed method can achieve better performance than the state-of-the-art methods. The source code and the pre-trained spectral-spatial diffusion model will be publicly available at <https://github.com/chenning0115/SpectralDiff>.

**Index Terms**—Deep neural network, hyperspectral image (HSI) classification, latent representation, feature extraction, diffusion model, deep generative model.

## I. INTRODUCTION

**H**YPERSPECTRAL imaging is a cutting-edge technology that enables the acquisition of high-resolution spectral information of imaged objects. By integrating spatial and spectral reflectance information, each pixel in a hyperspectral

image (HSI) corresponds to a unique spectral curve, providing rich information for identification and differentiation of diverse materials and surfaces. Beyond the limited perception of human eyes, the spectral detection range of hyperspectral imaging empowers a comprehensive understanding of nature [1], [2]. This technology has demonstrated significant potential in numerous fields, such as environmental management, agriculture, land management, ecology, geology, urban planning, and oceanography. HSI classification, which involves assigning pixels to specific land cover classes, such as soil and grass, is one of the most significant applications of hyperspectral imaging. As a fundamental component of hyperspectral data processing, HSI classification plays an indispensable role in most hyperspectral imaging applications [3], [4].

The high dimensionality of HSI poses a significant challenge for the accurate classification of pixels. With hundreds of spectral bands and massive amounts of data, it can be difficult to identify relevant features. To overcome this challenge, researchers have developed a range of methods to map spectral vectors from high-dimensional space to low-dimensional feature space in order to extract effective spectral features. These methods include classic statistical transformation techniques such as principal component analysis (PCA) [5], minimum noise fraction (MNF) [6], local preserving projection (LPP) [7], linear discriminant analysis (LDA) [8], independent component analysis (ICA) [9], and sparse preserving projection (SPP) [10]. However, the spatial heterogeneity and homogeneity of HSIs make it difficult to fully utilize them by extracting spectral features alone. To address this limitation, researchers have proposed a series of methods to jointly extract spatial and spectral features, such as extended mathematical contour (EMP) [11] and extended attribute contour (EAP) [12].

With the successful introduction and rapid development of deep neural networks (DNN) [13], [14], it has achieved outstanding performance in image classification [15], [16], image segmentation [17], [18], instance segmentation [19], and object detection [20], [21]. DNN offers a solution by offering an adaptable and potent framework for automatically learning complicated features and relationships in data [22]. The HSI classification accuracy has been steadily improved by a number of HSI spectral feature extraction techniques based on DNN. Due to the fact that HSI has both spectral and spatial features, some spectral-spatial feature extraction techniques combining DNN have been proposed in order to fully explore the three-dimensional data characteristics [23], including stacked auto-encoders [24], deep fully convolutional network [23], deep prototypical network [25], spatial pyramid pooling [26], and spectralformer [27].

This work has been submitted to the IEEE for possible publication. Copyright may be transferred without notice, after which this version may no longer be accessible.

This work was supported in part by the National Natural Science Foundation of China under Grant U22B2014, Grant 62101072 and Grant 42201481, in part by the Science and Technology Plan Project Fund of Hunan Province under Grant 2022RSC3064, in part by the Hunan Provincial Natural Science Foundation of China under Grant 2021JJ40570. (Ning Chen and Jun Yue contributed equally to this work.) (Corresponding author: Leyuan Fang.)

Ning Chen is with the Institute of Remote Sensing and Geographic Information System, Peking University, Beijing 100871, China (e-mail: chenning0115@pku.edu.cn).

Jun Yue is with the School of Automation, Central South University, Changsha 410083, China (e-mail: jyue@pku.edu.cn).

Leyuan Fang is with the College of Electrical and Information Engineering, Hunan University, Changsha 410082, China, and also with the Peng Cheng Laboratory, Shenzhen 518000, China (e-mail: fangleyuan@gmail.com).

Shaobo Xia is with the Department of Geomatics Engineering, Changsha University of Science and Technology, Changsha 410114, China (e-mail: shaobo.xia@ucalgary.edu.ca).

Despite the favorable outcomes achieved with DNN-based methods in HSI classification, these methods still have limited capability in globally modeling the spectral-spatial relationships across samples. Existing methods mainly use metric learning method to measure the distance between a pair of samples [28], or use graph neural network to model samples [29], [30]. Nevertheless, the use of metric learning methods fails to capture the global relationship between samples, while utilizing graph neural networks to gauge the global relationship among all samples may result in prohibitively high computational expenses and sluggish gradient descent [31]. Consequently, the ability of these methods to effectively model the relationship between samples is restricted to a particular subset of samples, thereby impeding their capacity to exploit the full spectrum of samples for relationship modeling.

In order to solve the above challenges, an HSI classification method with spectral-spatial diffusion models, namely SpectralDiff, is proposed. First, we directly feed hyperspectral cube data with spatial and spectral dimensions, and construct hyperspectral channel distribution in spectral-spatial latent feature space by spectral-spatial diffusion process, which is a Markov process consisting of both forward and reverse processes. During the forward process, Gaussian noise is added to the hyperspectral channel input data, while in the reverse process, the noise is removed through multiple time steps. By training a spectral-spatial denoising network to estimate the noise added during the forward process, we construct the joint distribution of hyperspectral channels to establish the global relationship between all samples. Next, we extract the spectral-spatial diffusion features from the spectral-spatial denoising network and feed them into the vision transformer module to directly generate image classification results. Our approach models the global relationship between samples and extracts the spectral-spatial diffusion features with diffusion models. The main contributions of this paper are as follows.

- We formulate the construction of global relationship between samples as a spectral-spatial diffusion process, which is the first study to apply the diffusion models to HSI classification to the best of our knowledge.
- We propose an HSI classification framework based on forward and reverse diffusion processes, which can directly generate spectral-spatial diffusion features with global information.
- Numerous experiments demonstrate the superiority of the proposed method over existing state-of-the-art techniques. Moreover, through ablation experiments, we validate the effectiveness of spectral-spatial diffusion features.

The rest of this article is structured as follows. In Section II, we provide a brief overview of the existing work on hyperspectral image classification and diffusion models. Section III outlines our proposed method in detail, highlighting the key components of our approach. In Section IV, we present the experimental setup and discuss our results from both qualitative and quantitative perspectives. Additionally, we validate the effectiveness of our approach through ablation experiments. Finally, in Section V, we summarize the conclusions of our study and provide insights into the future directions of research

in this field.

## II. RELATED WORK

In this section, we provide an introduction to the background and related work associated with our proposed method. Specifically, we discuss existing techniques for HSI classification based on traditional spectral-spatial feature extraction, as well as those based on deep learning. Furthermore, we present an overview of the diffusion model and its development context, highlighting the key advancements and challenges in this field. Through this exposition, we aim to establish a solid foundation for our proposed method and contextualize our contribution within the broader scope of HSI classification research.

### A. Hyperspectral Image Classification

Hyperspectral sensor captures both spatial and spectral information. In an HSI image, every pixel vector corresponds to a unique spectral curve. The primary objective of HSI image classification is to assign each pixel to a specific ground class, such as rivers, forests, lakes, farmland, buildings, grasslands, minerals, roads and rocks. Classification is a pivotal step in the application of HSI and has significant implications for environment, geology, mining, ecology, forestry, agriculture, and other areas [32], [4]. HSI classification enables quick and precise acquisition of ground feature, empowering informed decision-making and management. For instance, in agriculture, HSI classification can be used to track disease progression and crop development, improving crop quality and productivity. In the mining sector, HSI classification can make it easier to find and identify minerals, increasing the effectiveness of mining natural resources [3], [33].

Spectral feature extraction based on continuous spectral signals is widely used in HSI feature extraction, which considers each pixel of the HSI as an independent spectral vector and ignores the spatial relationships between pixels when generating the ground objects' features [34]. Linear feature extraction methods such as principal component analysis (PCA) [5], linear discriminant analysis (LDA) [8], and minimum noise fraction (MNF) [6], [35] are among the commonly used spectral feature extraction techniques. Nonetheless, the nonlinear nature of HSI has led to the development of numerous nonlinear feature extraction approaches in recent years, complementing the statistical transformation methods based on prior knowledge. In recent years, many nonlinear HSI feature extraction methods have been proposed [36], [1], including locality-preserving discriminant analysis (LFDA) [37], manifold learning [38], sparsity preserving projections (SPP) [39], improved manifold coordinate representations [40] and locality preserving projections (LPP) [7].

The HSI analysis technique involves extracting separable features of patterns from the spectral signal to reduce the dimensionality of the data. Despite its efficacy, this method alone cannot fully utilize the characteristics of HSI due to its spatial homogeneity and heterogeneity. Consequently, incorporating image texture and structural features is necessary to overcome this limitation. Researchers have proposed several methods to extract spatial structure and texture information

from HSIs to obtain spatial features such as three-dimensional gray-level cooccurrence [41] and discriminative Gabor feature selection [42]. In the domain of HSI feature extraction and classification, the classic spectral-spatial joint feature extraction methods include extended morphological profile [11], spatial and spectral regularized local discriminant embedding [43], extended attribute profile [12], spatial-spectral manifold alignment [44], directional morphological profiles [11], and spectral-spatial locality preserving projection [45].

Deep learning has emerged as a significant breakthrough in the field of machine learning, providing automatic feature learning from data [13]. HSI classification, in particular, benefits from deep learning models due to their ability to handle complex and nonlinear relationships between input data and output classes [16], leading to improved classification accuracy compared to traditional machine learning methods [46], [35]. To fully utilize the spectral-spatial features of HSI, joint spectral-spatial HSI feature extraction methods based on deep learning, such as recurrent neural network [47], deep residual network [48], [49], capsule networks [50], and transformer [27], have been proposed. While these methods have yielded satisfactory results, challenges remain, such as the inability to capture global relationships between samples. To address this issue, researchers have proposed using graph neural network to model the relationship between samples [29]. However, the use of graph neural network for global relationship modeling incurs high computing and memory costs, and slow gradient decline [31]. In this paper, we propose using a diffusion model to model the global relationship of samples and verify the effectiveness of this method through extensive comparative experiments.

### B. Diffusion Models

Diffusion models, also known as diffusion probabilistic models [51], belong to the class of latent variable models (LVM) in machine learning [52]. They draw inspiration from non-equilibrium thermodynamics and construct a Markov chain that gradually introduces random noise into the input data [53]. Subsequently, the Markov chain is trained utilizing variational inference [54], delivering remarkable performance across various domains such as natural language processing [55], [56], time series forecasting [57], [58], and molecular graph modeling [59], [60]. Currently, research on diffusion models is generally based on three primary paradigms [61], namely score-based generative models [62], [63], [64], stochastic differential equations (SDE) [65], [66], and denoising diffusion probabilistic models (DDPM) [67], [51].

The diffusion model aims to infer the underlying structure of a dataset by modeling the diffusion of data points in the latent space [68], which consists of two core processes: forward and reverse. During the forward process, the input data is gradually perturbed by introducing Gaussian noise in multiple time steps. Conversely, the reverse process aims to restore the original input data by reducing the discrepancy between the predicted noise and the increased noise in multiple reverse time steps. In the field of computer vision, this entails training a neural network to perform denoising of images that are blurred

by Gaussian noise, by learning the reverse diffusion process [69]. The diffusion model has gained popularity in recent times, owing to its remarkable flexibility and robustness, and has been successfully employed to address a diverse range of intricate visual challenges [54], such as image inpainting [70], image generation [53], [67], [66], [68], image-to-image translation [71], [72], [73], image fusion [69], and image super-resolution [74], [75], [76].

The feature representation learned from the diffusion models has been demonstrated to be highly effective in various discriminating tasks, such as image classification [77], object detection [78] and image segmentation [79], [80]. By constructing the distribution of input data, the diffusion model can effectively capture the underlying patterns and relationships between samples. In this paper, we extend the diffusion model to the spectral-spatial diffusion model, which can build the distribution of multi-channel input data and thereby establish the global relationship between samples. This enables the model to effectively learn and leverage the spatial and spectral information of the input data, leading to improved performance in HSI classification.

## III. METHODOLOGY

In this section, we provide a detailed description of the proposed SpectralDiff, as shown in Fig. 1. By training the spectral-spatial denoising network to estimate the noise added in the forward spectral-spatial diffusion process, we establish the global relationship among all samples.

### A. Spectral-Spatial Diffusion

Given an HSI  $\mathcal{H} \in \mathbb{R}^{H \times W \times B}$ , where  $H$  and  $W$  denote the height and width of  $\mathcal{H}$ , respectively.  $B$  represents the number of spectral channels. To learn the joint latent structure of images with hundreds of channels, we add noise to the spectral-spatial instance in the forward process, and eliminate the noise added by the forward process by training a spectral-spatial denoising network in the reverse process [67]. The purpose of training the diffusion model with forward and reverse processes is to learn the joint latent structure between hyperspectral channels by simulating the diffusion of hyperspectral channels in the latent space [64], [81].

1) *Forward Spectral-Spatial Diffusion Process*: The forward spectral-spatial diffusion process, drawing inspiration from the principles of non-equilibrium thermodynamics, can be considered a Markov chain [53], [67]. Its progressive stages entail the gradual incorporation of Gaussian noise into the data. In this study, we extract spectral-spatial instance  $\mathcal{HI} \in \mathbb{R}^{K \times K \times B}$  using a  $K \times K$  neighborhood from the whole HSI  $\mathcal{H}$ . The forward spectral-spatial diffusion process is distinguished by the “no memory” property, whereby the probability distribution of the HSI at a given time  $t + 1$  is exclusively determined by its state at time  $t$ . At the  $t$ th step, the spectral-spatial instance imbued with noise is expressed as follows:

$$P(\mathcal{HI}_t | \mathcal{HI}_{t-1}) = \mathcal{N}(\mathcal{HI}_t; \sqrt{\alpha_t} \mathcal{HI}_{t-1}, (1 - \alpha_t) \mathbf{I}) \quad (1)$$

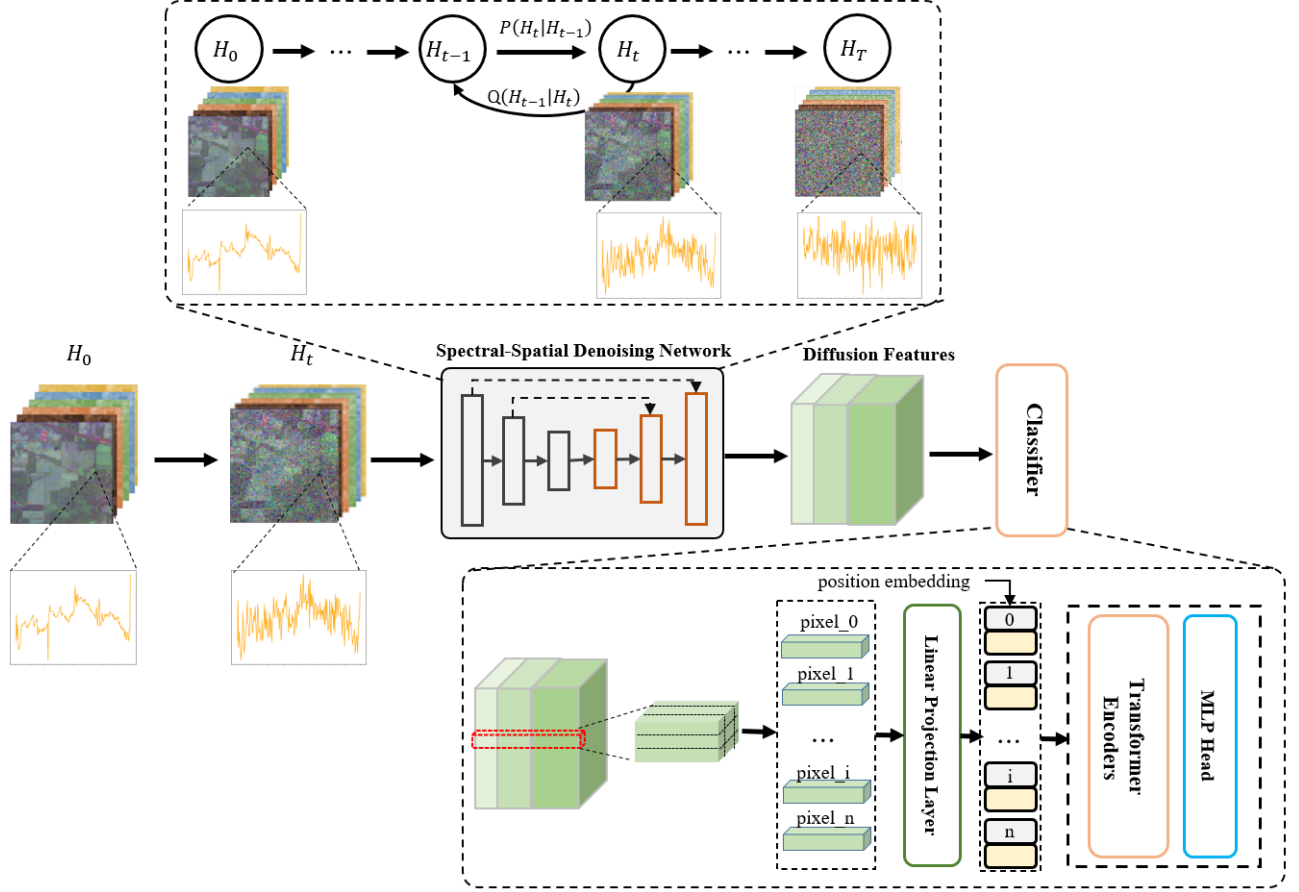


Fig. 1: Overview of the proposed SpectralDiff.  $\mathcal{H}_0$  and  $\mathcal{H}_t$  represent hyperspectral images of timestep 0 and timestep  $T$ , respectively.  $P(\cdot|\cdot)$  and  $Q(\cdot|\cdot)$  represent the forward and reverse spectral-spatial diffusion process, respectively.

where  $\mathcal{H}\mathcal{I}_{t-1}$  and  $\mathcal{H}\mathcal{I}_t$  denote the noisy hyperspectral instances at timestep  $t-1$  and  $t$ , respectively.  $\mathbf{I}$  stands for the standard normal distribution.  $\sqrt{\alpha_t}\mathcal{H}\mathcal{I}_{t-1}$  and  $(1-\alpha_t)\mathbf{I}$  denote the mean and variance of  $P(\mathcal{H}\mathcal{I}_t|\mathcal{H}\mathcal{I}_{t-1})$ , respectively. The variance of Gaussian noise added at timestep  $t$  is controlled by a variance schedule referred to as  $\alpha_t$ . The magnitude of the added Gaussian noise decreases as the value of  $\alpha_t$  increases. By Eq. (1), we can derive the expression of  $\mathcal{H}\mathcal{I}_1 \in \mathbb{R}^{K \times K \times B}$  during the first diffusion as follows:

$$\mathcal{H}\mathcal{I}_1 = \sqrt{\alpha_1}\mathcal{H}\mathcal{I}_0 + \sqrt{1-\alpha_1}\epsilon \quad (2)$$

where  $\mathcal{H}\mathcal{I}_0$  stands for the hyperspectral instance before diffusion.  $\epsilon \in \mathbb{R}^{K \times K \times B}$  is the added Gaussian noise. By using Eq. (1) and Eq. (2), the expression of  $\mathcal{H}\mathcal{I}_t$  can be derived as follows:

$$\begin{cases} \mathcal{H}\mathcal{I}_t = \sqrt{\bar{\alpha}_t}\mathcal{H}\mathcal{I}_0 + \sqrt{1-\bar{\alpha}_t}\epsilon \\ \bar{\alpha}_t = \prod_{i=1}^t \alpha_i \end{cases} \quad (3)$$

where  $\bar{\alpha}_t$  represents the product of  $\alpha_1$  to  $\alpha_t$ . The computation of  $\mathcal{H}\mathcal{I}_t$  in the context of forward spectral-spatial diffusion process hinges upon the timestep  $t$ , variance schedule  $\alpha_1, \dots, \alpha_t$ , and the noise sampled from the standard normal

distribution. Given these inputs, the hyperspectral instance at timestep  $t$  can be directly generated by Eq. (3).

2) *Reverse Spectral-Spatial Diffusion Process*: In the process of reverse spectral-spatial diffusion, a spectral-spatial denoising network is trained to gradually denoise the noisy hyperspectral instance to obtain the original hyperspectral instance  $\mathcal{H}\mathcal{I}_0$  [79]. In the  $t$ -th step of the reverse diffusion process, denoising operation is performed on the noisy hyperspectral instance  $\mathcal{H}\mathcal{I}_t$  to obtain the hyperspectral instance of the previous step, which is  $\mathcal{H}\mathcal{I}_{t-1}$ . Given the hyperspectral instance at step  $t$ , the conditional probability of the hyperspectral instance at step  $t-1$  can be expressed as follows [67], [82]:

$$Q(\mathcal{H}\mathcal{I}_{t-1}|\mathcal{H}\mathcal{I}_t) = \mathcal{N}(\mathcal{H}\mathcal{I}_{t-1}; \mu_\theta(\mathcal{H}\mathcal{I}_t, t), \sigma_t^2 \mathbf{I}) \quad (4)$$

where  $\mu_\theta(\mathcal{H}\mathcal{I}_t, t)$  and  $\sigma_t^2$  denote the mean and variance of the condition distribution  $Q(\mathcal{H}\mathcal{I}_{t-1}|\mathcal{H}\mathcal{I}_t)$ , respectively. The variance is determined by the variance schedule, which can be expressed as follows:

$$\sigma_t^2 = \frac{1-\bar{\alpha}_{t-1}}{1-\bar{\alpha}_t}(1-\alpha_t) \quad (5)$$

To obtain the mean of the conditional distribution  $Q(\mathcal{H}\mathcal{I}_{t-1}|\mathcal{H}\mathcal{I}_t)$ , we need to train the network to predict the

added noise. The mean can be represented as follows:

$$\mu_\theta(\mathcal{HI}_t, t) = \frac{1}{\sqrt{\alpha_t}}(\mathcal{HI}_t - \frac{1 - \alpha_t}{\sqrt{1 - \alpha_t}}\epsilon_\theta(\mathcal{HI}_t, t)) \quad (6)$$

where  $\epsilon_\theta(\cdot, \cdot)$  denote the spectral-spatial denoising network whose input is the timestep  $t$  and the noisy hyperspectral instance  $\mathcal{I}_t$  at timestep  $t$ .

### B. Loss Function of Spectral-Spatial Diffusion Process

For the spectral-spatial denoising network training, the hyperspectral instance  $\mathcal{HI}_0^i \in \mathbb{R}^{K \times K \times B}$  are first extracted, followed by sampling the noise matrix  $\epsilon^i \in \mathbb{R}^{K \times K \times B}$  of equivalent size from the standard normal distribution. Subsequently, the timestep  $t$  is sampled from a uniform distribution  $U(\{1, \dots, T\})$ . With the above-mentioned sampling completed, the noisy hyperspectral instance at timestep  $t$  can be calculated by Eq. (3). The noisy hyperspectral instance and timestep are fed into the spectral-spatial denoising network to generate the predicted noise. The loss function of the spectral-spatial diffusion process can be expressed as follows:

$$\begin{aligned} \mathcal{L}_{ssdp} &= \sum_{i=1}^N \left\| \epsilon^i - \epsilon_\theta(\mathcal{HI}_t^i, t) \right\|_1 \\ &= \sum_{i=1}^N \left\| \epsilon^i - \epsilon_\theta(\sqrt{\alpha_t} \mathcal{HI}_0^i + \sqrt{1 - \alpha_t} \epsilon, t) \right\|_1 \end{aligned} \quad (7)$$

where  $N$  and  $i$  represent the total number of hyperspectral instances and the index of a hyperspectral instance.

### C. Structure of the Spectral-Spatial Denoising Network

In order to predict the noise added in the forward spectral-spatial diffusion process, the structure of the spectral-spatial denoising network adopts a structure similar to U-Net [74], as shown in Fig. 2. The image with noise undergoes a 3D convolution layer and three 3D down-sampling blocks to achieve spectral and spatial feature encoding. Subsequently, it is decoded via three 3D up-sampling blocks and another 3D convolution layer to generate the output. Unlike diffusion model processing RGB images, the Spectral-Spatial Denoising Network employs 3D convolution structures for the efficient extraction of spectral and spatial information simultaneously during down-sampling and up-sampling processes. To extract the diffusion feature of every pixel in both encoder and decoder processes, we preserved the spatial dimensions while compressing and restoring the spectral dimensions. The internal structures of 3D down-sampling and 3D up-sampling blocks are depicted in Fig. 2(b) and Fig. 2(c), respectively, consisting of two layer blocks that incorporate a 3D-convolution layer, a BatchNorm3D layer, and a ReLU activation layer. The down-sampling structure applies a 3D convolution structure with stride=2 for gradually reducing the spectral dimension, while the up-sampling block applies a 3-D deconvolutional layer with stride=2 to gradually restore the spectral dimension.

### D. Classification with Spectral-Spatial Diffusion Features

After the spectral-spatial denoising network has been trained, we feed the spectral-spatial instance with noise into the classification stage to generate the spectral-spatial diffusion features that contain global spectral-spatial information. The spectral-spatial diffusion features are activation tensors extracted from the spectral-spatial denoising network as shown in Fig. 2(a). We feed these features into the spectral vision transformer for final classification. The spectral vision transformer conducts self-attention operations in various positions while using the spatial position for position embedding. The structure of the spectral vision transformer is shown in Fig. 1.

## IV. EXPERIMENTS

### A. Experimental Settings

1) *Datasets*: In order to verify the effectiveness of our algorithm, we applied the algorithm to three public datasets: the Indian Pines dataset, the Pavia University dataset, and the Houston 2013 dataset.

The Indian Pines dataset was collected in 1992 using the Airborne Visible/Infrared Imaging Spectrometer (AVIRIS) Sensor, covering the northwestern region of Indiana in the United States. Comprising of 224 spectral bands, the uncorrected dataset spans a range of 0.4 to 2.5  $\mu\text{m}$  and is composed of 145  $\times$  145 pixels with a spatial resolution of 20 meters. It contains 16 different land-cover classes. For the purpose of experimentation, 24 water-absorption bands and noise bands were removed, and a subset of 200 bands were selected for our analysis.

The Pavia University dataset was collected in 2001 by the Reflective Optics System Imaging Spectrometer (ROSIS) Sensor, covering the Pavia University in Northern Italy. It contains of 115 spectral bands while 12 noise bands were removed so that 103 bands were used. It is composed of 610  $\times$  340 pixels with a spatial resolution of 1.3 m. The dataset covers Nine categories.

The Houston 2013 dataset was provided by the Hyperspectral Image Analysis Group and the NSF-funded Airborne Laser Mapping Center (NCALM) at the University of Houston, US. Originally used for scientific purposes in the 2013 IEEE GRSS Data Fusion Competition. It consists of 144 spectral bands ranging from 0.38 to 1.05  $\mu\text{m}$  and a spatial resolution of 2.5 m. The dataset has 349  $\times$  1905 pixels and has been labeled into 15 distinct classes.

Table I shows the size of the training and testing datasets used in this experiment, including the sample distribution of each land cover category. For Indian Pines, Pavia University, and Houston datasets, 10%, 5%, and 10% were respectively sampled as the training sample sets.

2) *Evaluation Metrics*: We will compare the effectiveness of our algorithm with other algorithms from four aspects, mainly including OA, AA,  $\kappa$ , and the classification accuracy of each land cover category itself.

3) *Training Details*: The PyTorch training framework was utilized to implement and train the model, with the basic hardware environment comprising an AMD EPYC 7543

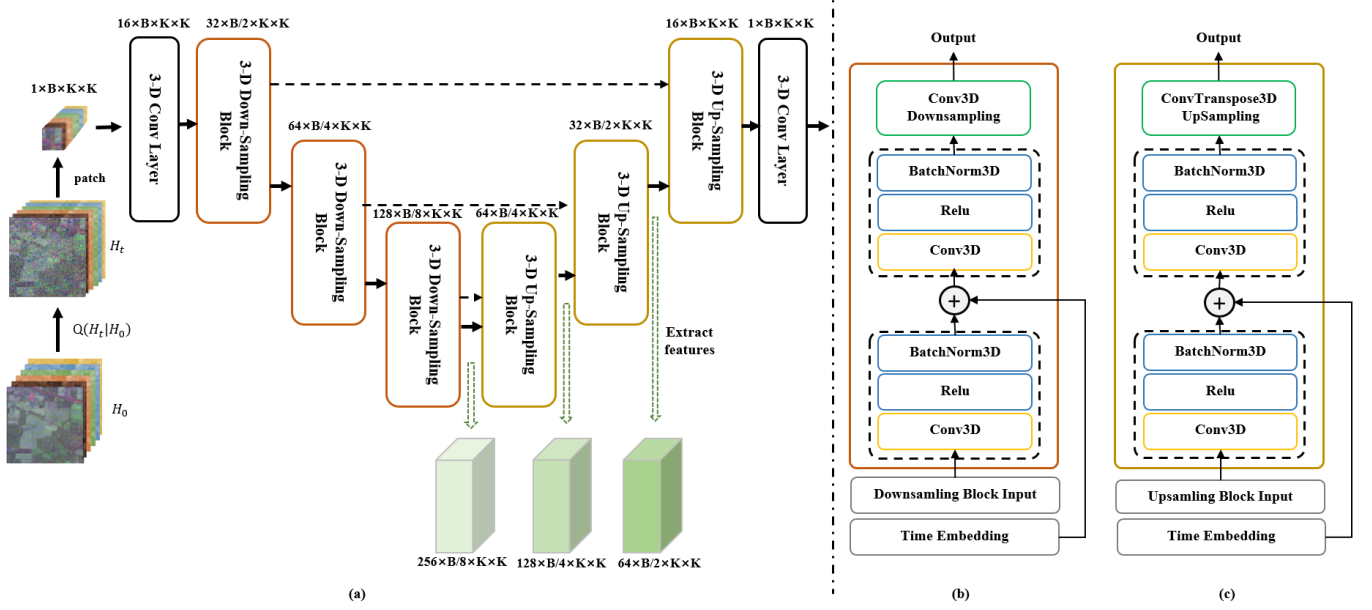


Fig. 2: Structure of the spectral-spatial denoising network. (a) The network consists of three 3-D down-sampling blocks and three 3-D up-sampling blocks. (b) The details of the 3-D down-sampling block. (c) The details of the 3-D up-sampling block.

TABLE I  
TRAINING AND TEST SAMPLE NUMBERS IN THE INDIAN PINES DATASET, THE PAVIA UNIVERSITY DATASET, AND THE HOUSTON 2013 DATASET.

NO.	Indian Pines			Pavia University			Houston 2013		
	Class	Training.	Test.	Class	Training.	Test.	Class	Training.	Test.
1	Alfalfa	3	43	Asphalt	340	6291	Healthy grass	133	1118
2	CornMotill	146	1282	Meadows	918	17731	Stressed grass	123	1131
3	CornMintill	77	753	Gravel	105	1994	Synthetic grass	72	625
4	Corn	21	216	Trees	147	2917	Trees	125	1119
5	GrassPasture	33	450	PaintedMetalSheets	64	1281	Soil	125	1117
6	GrassTrees	72	658	BareSoil	258	4771	Water	33	292
7	GrassPastureMowed	7	21	Bitumen	67	1263	Residential	116	1152
8	HayWindrowed	37	441	SelfBlockingBricks	198	3484	Commercial	117	1127
9	Oats	2	18	Shadows	41	906	Road	138	1114
10	SoybeanNotill	88	884				Highway	107	1120
11	SoybeanMintill	275	2180				Railway	126	1109
12	SoybeanClean	49	544				Parking Lot 1	122	1111
13	Wheat	23	182				Parking Lot 2	60	409
14	Woods	140	1125				Tennis Court	43	385
15	BuildingsGrassTreesDrives	41	345				Running Track	62	598
16	StoneSteelTowers	10	83						
	Total	1024	9225	Total	2138	40638	Total	1502	13527

production-grade CPU, 128GB of memory, and two NVIDIA GeForce RTX 3090 GPUs, each with 24GB of memory.

The diffusion model was optimized using the Adam optimizer, with a learning rate of  $1e-4$ , a batch size of 256, and a patch size of 16. The number of training epochs was determined based on the loss metric, and the training process was terminated when the loss function no longer decreased substantially. The training process for the Indian Pines, Pavia, and Houston datasets was stopped at 30,000, 3,000, and 3,000 epochs, respectively. The classification model was trained using an Adam optimizer, with a learning rate of  $1e-3$  and a

smaller batch size of 64. Empirically, it was observed that this model converged rapidly, and around 20 epochs were sufficient to attain the desired results for all three datasets.

### B. Performance Analysis

In order to compare the effectiveness of the proposed approach, several representative algorithms were selected for the control experiments, including:

- 1) K-nearest neighbors (KNN) algorithm, where  $K=5$  was found to be the optimal hyperparameter value through experiments.

TABLE II

QUANTITATIVE PERFORMANCE OF DIFFERENT CLASSIFICATION METHODS IN TERMS OF OA, AA, AND  $\kappa$ , AS WELL AS THE ACCURACIES FOR EACH CLASS ON THE INDIAN PINES DATASET. THE BEST ONE IS SHOWN IN BOLD

Class	Conventional Classifiers			Classic Backbone Networks			miniGCN [31]	SpectralFormer [27]	SpectralDiff
	KNN	RandomForest	SVM	1-D CNN [36]	2-D CNN [83]	3-D CNN [84]			
1	4.65	16.28	39.53	20.93	58.14	9.30	16.28	18.18	<b>79.07</b>
2	59.83	67.55	78.71	76.29	55.93	77.30	57.33	95.24	<b>98.83</b>
3	40.90	49.80	66.53	58.96	79.28	61.75	56.71	90.53	<b>98.41</b>
4	21.76	24.54	53.70	48.61	51.85	31.02	40.28	92.24	<b>94.44</b>
5	74.44	76.89	82.67	76.00	89.33	80.00	85.11	<b>98.62</b>	94.89
6	97.11	94.83	96.66	96.35	93.92	96.96	97.26	98.78	<b>100.00</b>
7	90.48	61.90	85.71	80.95	95.24	90.48	85.71	7.41	<b>100.00</b>
8	98.19	95.01	95.69	97.05	97.96	<b>100.00</b>	98.64	99.77	99.09
9	5.56	11.11	50.00	16.67	<b>61.11</b>	16.67	5.56	29.41	44.44
10	62.56	64.59	73.30	68.44	82.81	70.14	86.09	91.51	<b>97.51</b>
11	74.95	88.49	84.13	82.57	98.99	91.70	60.96	87.45	<b>99.17</b>
12	18.01	45.22	71.51	66.73	68.20	56.43	81.25	91.37	<b>97.79</b>
13	91.21	95.60	98.90	97.80	83.52	96.15	98.35	98.31	<b>99.45</b>
14	95.11	95.91	92.18	94.93	97.16	97.42	88.44	96.16	<b>99.56</b>
15	13.62	33.62	59.13	63.48	83.77	79.13	55.65	89.85	<b>99.13</b>
16	81.93	79.52	89.16	89.16	83.13	62.65	96.39	<b>98.77</b>	91.57
OA(%)	67.07	74.64	80.93	78.78	84.53	81.41	72.75	92.22	<b>98.34</b>
AA(%)	58.14	62.55	76.09	70.93	80.02	69.82	69.38	80.22	<b>93.33</b>
$\kappa * 100$	61.99	70.68	78.19	75.66	82.19	78.60	69.44	91.14	<b>98.11</b>

TABLE III

QUANTITATIVE PERFORMANCE OF DIFFERENT CLASSIFICATION METHODS IN TERMS OF OA, AA, AND  $\kappa$ , AS WELL AS THE ACCURACIES FOR EACH CLASS ON THE PAVIA UNIVERSITY DATASET. THE BEST ONE IS SHOWN IN BOLD

Class	Conventional Classifiers			Classic Backbone Networks			miniGCN [31]	SpectralFormer [27]	SpectralDiff
	KNN	RandomForest	SVM	1-D CNN [36]	2-D CNN [83]	3-D CNN [84]			
1	84.45	88.92	92.56	95.87	97.01	93.72	90.49	96.49	<b>99.59</b>
2	96.46	97.92	97.99	99.14	94.69	98.91	95.60	99.41	<b>99.99</b>
3	55.77	58.93	76.08	51.15	72.92	75.33	93.78	86.41	<b>99.45</b>
4	77.13	85.84	93.83	83.06	97.50	96.02	97.26	<b>97.81</b>	95.47
5	98.67	97.50	98.83	98.28	<b>100.00</b>	99.61	99.22	99.22	99.84
6	55.65	63.22	85.03	74.79	99.52	98.20	77.66	99.58	<b>100.00</b>
7	79.33	72.21	80.92	40.46	85.59	79.49	83.29	86.70	<b>99.29</b>
8	85.73	89.64	91.30	93.40	92.14	94.66	40.33	88.61	<b>99.80</b>
9	99.67	99.23	99.78	99.34	96.36	99.23	<b>100.00</b>	98.79	97.24
OA(%)	85.12	88.18	93.22	89.93	94.45	95.72	87.82	96.88	<b>99.48</b>
AA(%)	81.43	83.71	90.70	81.72	92.86	92.80	86.40	94.78	<b>98.96</b>
$\kappa * 100$	79.82	84.02	90.96	86.36	92.71	94.32	83.86	95.87	<b>99.30</b>

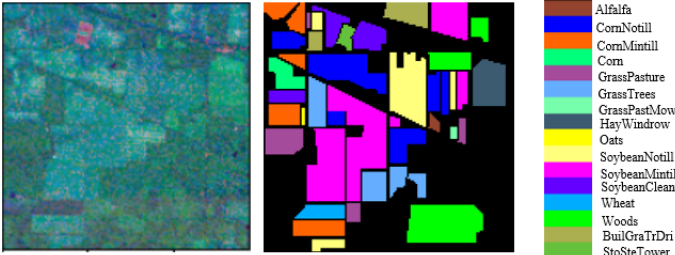


Fig. 3: The false-color composite image, the corresponding ground-truth map, and the legend of the Indian Pines dataset.

- 2) Random forest algorithm (RF), with 200 decision trees and entropy as the split criterion.

- 3) Support vector machine (SVM) algorithm with a radial basis function (RBF) kernel. The optimal values for the two kernel parameters  $\sigma$  and  $\lambda$  were selected through cross-validation, where  $\sigma$  was searched in the range  $[2^{-3}, 2^{-2}, \dots, 2^4]$ , and was searched in the range  $[10^{-2}, 10^{-1}, \dots, 10^4]$ .
- 4) 1-D CNN [36], consisting of 5 layers: a 1-D convolutional layer, a batch normalization (BN) layer, a rectified linear unit (ReLU) layer, an average pooling layer, and an output layer.
- 5) 2-D CNN [83], consisting of three 2-D convolutional blocks, each of which contains a 2-D convolutional layer, a BN layer, and a ReLU activation function. Each 2-D convolutional block has 8, 16, and 32  $3 \times 3$  2-D

TABLE IV  
QUANTITATIVE PERFORMANCE OF DIFFERENT CLASSIFICATION METHODS IN TERMS OF OA, AA, AND  $\kappa$ , AS WELL AS THE ACCURACIES FOR EACH CLASS ON THE HOUSTON 2013 DATASET. THE BEST ONE IS SHOWN IN BOLD

Class	Conventional Classifiers			Classic Backbone Networks			miniGCN [31]	SpectralFormer [27]	SpectralDiff
	KNN	RandomForest	SVM	1-D CNN [36]	2-D CNN [83]	3-D CNN [84]			
1	95.71	94.90	95.26	95.71	91.95	95.26	99.37	99.91	<b>100.00</b>
2	98.23	96.64	98.32	99.03	<b>100.00</b>	98.23	86.38	99.38	99.73
3	98.56	98.24	99.52	99.20	99.52	96.64	98.40	97.28	<b>99.68</b>
4	98.39	99.02	99.37	99.46	98.39	98.75	93.48	96.25	<b>99.82</b>
5	97.49	97.40	97.76	97.31	97.85	98.30	97.22	99.28	<b>100.00</b>
6	90.75	91.78	93.15	94.18	83.90	85.96	<b>98.63</b>	89.38	95.89
7	85.94	90.71	88.80	89.67	89.50	92.80	59.20	92.97	<b>98.09</b>
8	77.73	83.14	65.31	54.92	93.70	92.01	90.24	93.97	<b>97.69</b>
9	78.55	84.20	82.76	82.50	93.00	91.56	57.63	94.34	<b>96.95</b>
10	84.38	84.64	84.82	76.61	87.77	94.38	87.32	95.45	<b>100.00</b>
11	76.65	81.88	83.14	75.02	94.32	88.46	76.74	97.84	<b>99.73</b>
12	71.20	74.62	77.59	64.72	87.49	92.89	90.28	97.03	<b>97.57</b>
13	19.32	36.19	41.32	60.39	87.78	84.11	42.30	66.01	<b>93.15</b>
14	96.36	95.84	99.22	97.92	95.58	97.40	98.44	96.62	<b>100.00</b>
15	98.49	96.66	99.16	99.00	99.33	99.16	99.50	<b>100.00</b>	100.00
OA(%)	85.89	88.21	87.48	84.87	93.63	94.20	84.59	95.73	<b>98.82</b>
AA(%)	84.52	87.06	87.03	85.71	93.34	93.73	85.01	94.38	<b>98.55</b>
$\kappa * 100$	84.72	87.24	86.46	83.66	93.11	93.72	83.34	95.38	<b>98.73</b>

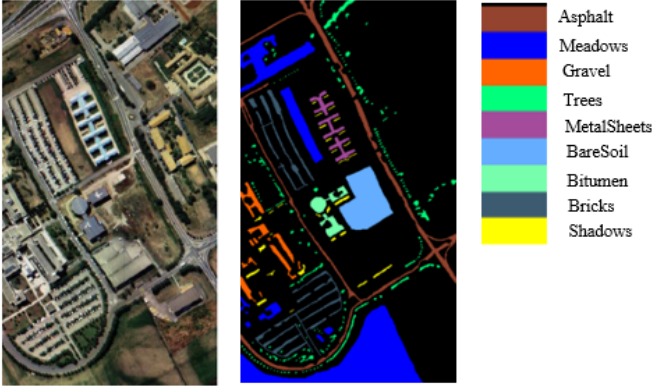


Fig. 4: The false-color composite image, the corresponding ground-truth map, and the legend of the Pavia University dataset.

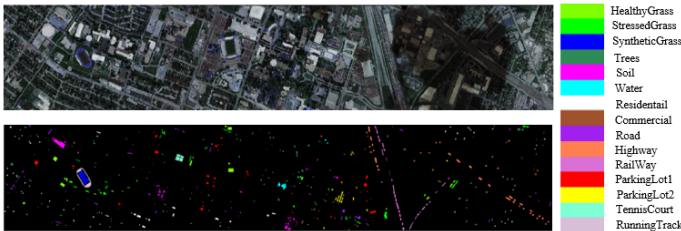


Fig. 5: The false-color composite image, the corresponding ground-truth map, and the legend of the Houston 2013 dataset.

filters, respectively.

- 6) 3-D CNN [84], consisting of three 3-D convolutional blocks, each of which contains a 3-D convolutional layer, a BN layer, a ReLU activation function and an

average pooling layer. Each 3-D convolutional block has 8, 16, and 32  $3 \times 3 \times 3$  3-D filters, respectively.

- 7) miniGCN [31], a variant of graph convolutional networks (GCN) that aims to address the challenges of high computational cost, full-batch network learning, and the inability to predict new input samples without retraining the network. MiniGCN is designed to train large-scale GCNs in a mini-batch fashion, making it more efficient and flexible than traditional GCNs.
- 8) SpectralFormer [27], feeding a 64-unit embedded spectrum into a sequence of five transformer encoder blocks. Each block comprises of a four-headed self-attention layer, an eight-hidden dimension MLP, and a GELU nonlinear activation layer. A dropout layer is used to inhibit 10% of neurons after encoding positional embeddings and within MLPs. We use the CAF version of spectralFormer while setting the patches to 7 and band patches to 3.
- 9) SpectralDiff: Our proposed model follows the basic architecture described earlier, comprising two stages: diffusion model training and classification. During diffusion model training, the input data is divided into  $16 \times 16$  patches, which are first passed through a 3D convolution layer with a kernel size of (3,3,3) and padding size of (1,1,1). Subsequently, three 3D down-sampling and three 3D up-sampling layers are employed for further spatial and spectral feature extraction. Finally, another 3D convolution layer with a kernel size of (3,3,3) and padding size of (1,1,1) will be passed. To extract diffusion features, we performed spatial and spectral reconstruction with noise images and timestamps as inputs. We used the output of U-net down-sampling and up-sampling layers while reducing its dimensionality to serve as diffusion

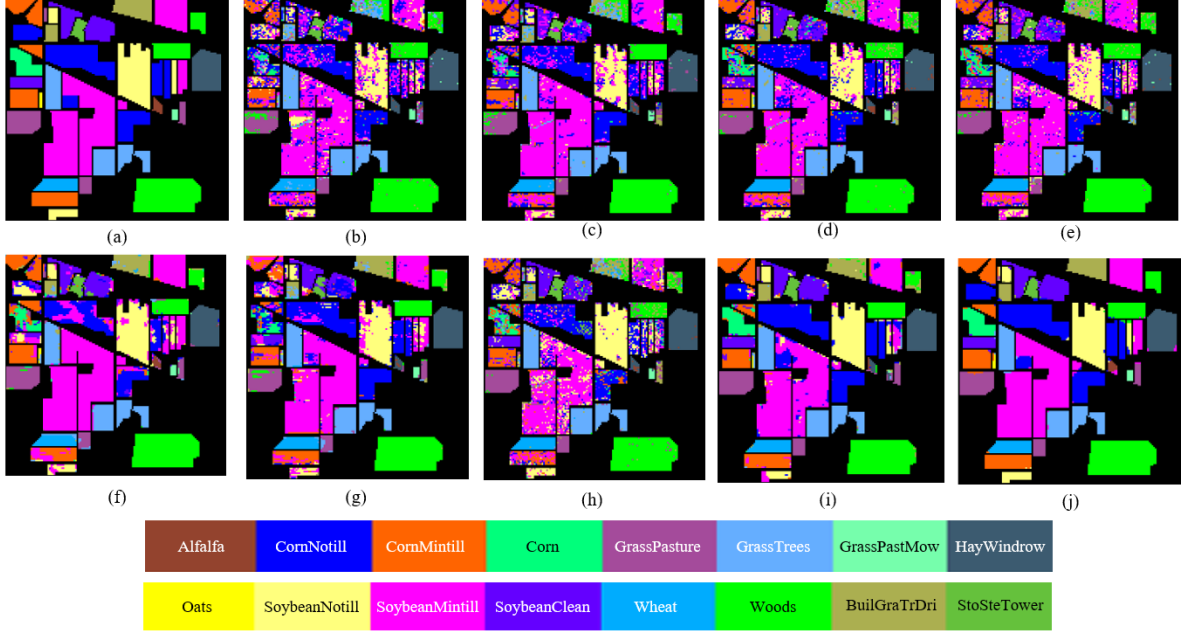


Fig. 6: Classification maps of the Indian Pines dataset. (a) Ground-truth map. (b) KNN (OA = 67.07%). (c) RandomForest (OA = 74.64%). (d) SVM (OA = 80.93%). (e) 1-D-CNN (OA = 78.78%). (f) 2D-CNN (OA = 84.53%). (g) 3-D-CNN (OA = 81.41%). (h) miniGCN (OA = 72.75%). (i) SpectralFormer (OA = 92.22%). (j) SpectralDiff (OA = 98.34%).

features. In this study, PCA was used. During training of the classification model, diffusion features undergo one linear mapping layer, five transformer block layers, and are finally linked to an MLP layer. Each transformer block comprises of one 4-head Self-Attention (SA) layer and one MLP layer.

1) *Quantitative Results:* Tables II-IV presents the classification results of three datasets, namely Indian Pines, Pavia University and Houston 2013, including OA, AA,  $\kappa$  and classification accuracy of each category. The optimal results are highlighted in bold. Notably, our proposed SpectralDiff algorithm shows superior performance in terms of OA, AA,  $\kappa$  and accuracy of multiple categories on all three datasets.

The table reveals that Conventional Classifiers, such as KNN, RF and SVM, have relatively poor performance due to their weak feature extraction ability. Shallow models struggle in effectively capturing spatial and spectral features, especially when dealing with hyperspectral images containing abundant spectral data. Among the three classifiers, SVM exhibits the best performance.

On the other hand, Classic Backbone Networks exhibit slightly better classification performance than Conventional Classifiers by leveraging deep neural networks to enhance the ability of feature extraction for spectral and spatial features. Nevertheless, this method is weaker than the Transformer-based model, even though it has a similar effect to miniGCN. Among the three classic backbone networks, the 3-D CNN model performs best on the Pavia University dataset and the Houston 2013 dataset, while the 2-D CNN model excels on the Indian Pines dataset. The 3-D CNN has a slightly weaker performance than the 2-D CNN.

Our study shows that the Transformer-based model, which includes SpectralFormer and SpectralDiff, outperforms other models because of its powerful fitting ability. Specifically, our proposed SpectralDiff model performs better than SpectralFormer since the diffusion model enhances the ability to extract deep spectral features and construct mutual relationships between different pixels. Additionally, based on the features extracted by the diffusion model, our improvement to the classification model also enhances the final classification performance.

Through the analysis of the classification performance of each detailed category, it can be found that SpectralDiff performs significantly better than other models for challenging categories, such as small sample categories. For example, on the Indian Pines dataset, SpectralDiff Model achieves the best classification results for categories like Alfalfa, Grass-PastureMowed, and Oats. Moreover, in all three datasets, SpectralDiff Model shows the most significant improvement in the AA index. This can be attributed to SpectralDiff Model's unique feature: pretraining all pixels, constructing mutual relationships between different pixels, and embedding their correlation into a new feature space. Compared to the reference method, the novel feature space expands the feature boundary to improve the model's generalization ability in subsequent classifier training.

2) *Qualitative results:* Figs. 6-8 display the classification results of Indian Pines, Pavia University, and Houston 2013. Visually, the SpectralDiff exhibits lower noise levels and closely aligns with the Ground Truth. Traditional classification algorithms produce noisy classification maps with discontinuous land cover blocks and rough classification results. Mean-

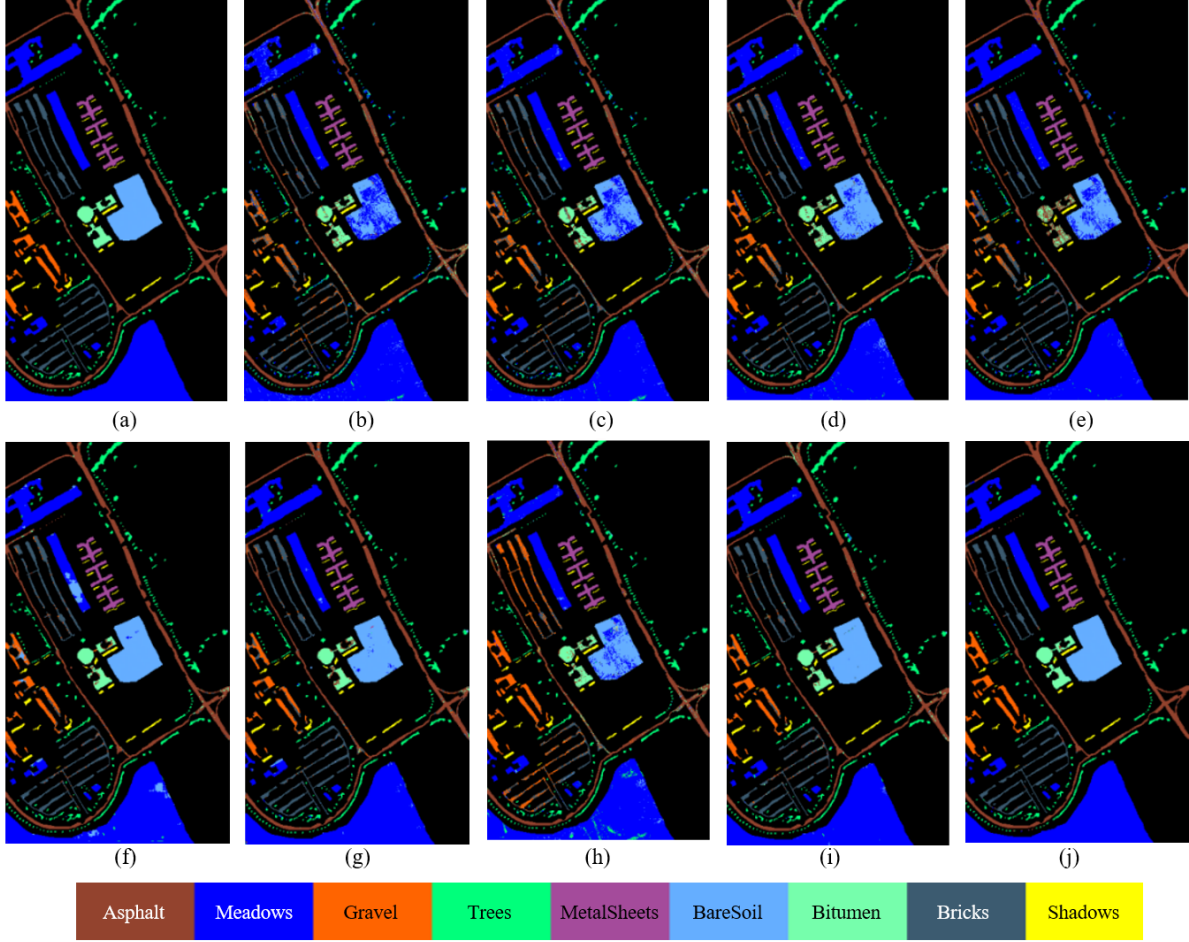


Fig. 7: Classification maps of the Pavia University dataset. (a) Ground-truth map. (b) KNN (OA = 85.12%). (c) RandomForest (OA = 88.18%). (d) SVM (OA = 93.22%). (e) 1-D-CNN (OA = 89.93%). (f) 2D-CNN (OA = 94.45%). (g) 3-D-CNN (OA = 95.72%). (h) miniGCN (OA = 87.82%). (i) SpectralFormer (OA = 96.88%). (j) SpectralDiff (OA = 99.48%).

while, Classic Backbone Networks provide better classification results with a reduction in noise points. Furthermore, the classification results of transformer-based model are visually improved and SpectralDiff shows a better overall performance in land cover classification compared to SpectralFormer.

The figure shows that for the SoybeanMintill class (purple area) in the Indian Pines dataset, compared to other methods, SpectralDiff has the almost complete coverage and no visible noise points. SpectralDiff has also accurately classified Asphalt (brown area) in the Pavia University dataset. The Houston dataset demonstrates that SpectralDiff has better performance in terms of clearer delineation and overall accuracy for Residential (white area) classification. Our analysis demonstrates that SpectralDiff notably improves the continuity and integrity of land cover classification, and this improvement is attributed to its superior ability to perform global macro feature extraction during pre-training. However, this improvement can lead to a loss of detail. For instance, the Houston dataset exhibits some changes in road morphology.

### C. Model Analysis

1) *Ablation study*: We further analyzed the benefits of the SpectralDiff Model, which involves feeding the original spectral features and the features extracted from the pre-training process with the diffusion model into our proposed transformer model. As shown in Table V, the classification results on Indian Pines, Pavia University, and Houston datasets are presented. The results demonstrate that using diffusion features as input significantly outperforms the use of raw features on all three datasets, resulting in improved OA, AA, and  $\kappa$  metrics. Notably, the improvement is most significant in terms of AA, with an increase of approximately 4% on the IP dataset, 1% on the PU dataset, and 2% on the HU dataset. This phenomenon aligns with our earlier discussion that the SpectralDiff Model performs significantly better than other models on challenging classes (small-sample classes) in terms of classification performance.

2) *Diffusion Model Analysis*: We further analyzed the effects of the diffusion model on the final classification model. Firstly, to verify the diffusion model effectiveness, we used the well-trained diffusion model to recover and reconstruct the spectral curves of the hyperspectral data. As an exam-

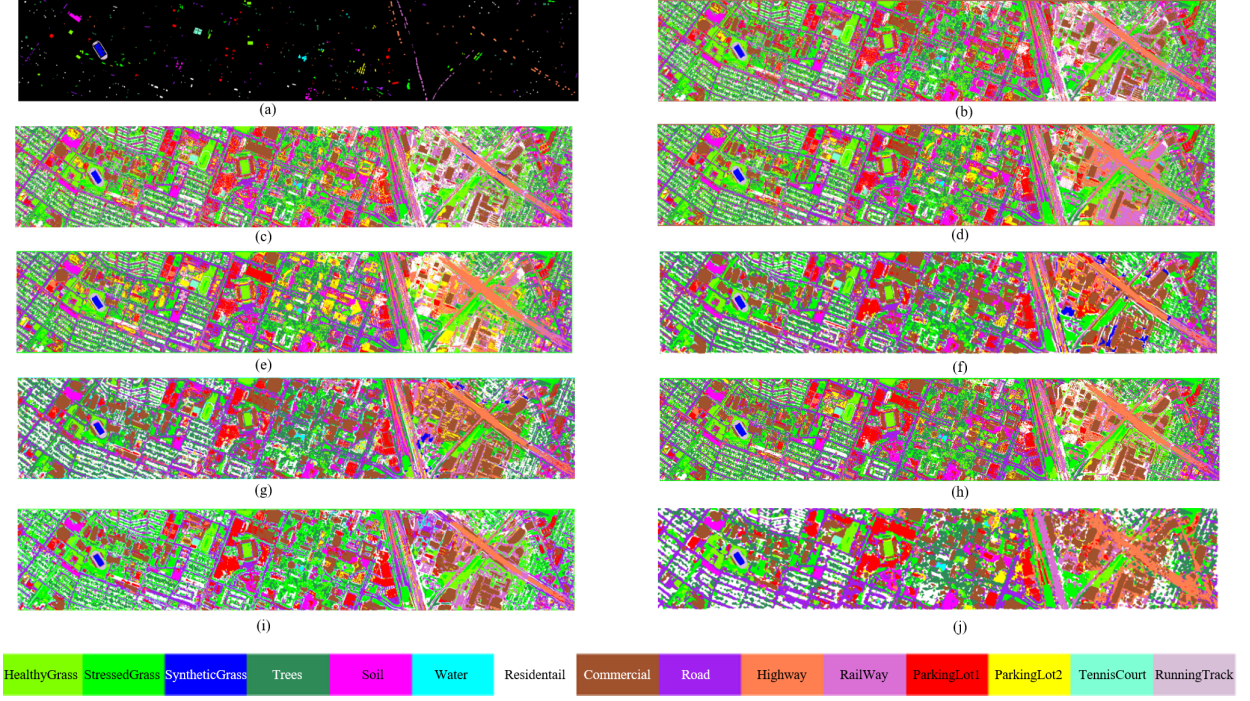


Fig. 8: Classification maps of the Houston 2013 dataset. (a) Ground-truth map. (b) KNN (OA = 85.89%). (c) RandomForest (OA = 88.21%). (d) SVM (OA = 87.48%). (e) 1-D-CNN (OA = 84.87%). (f) 2D-CNN (OA = 93.63%). (g) 3-D-CNN (OA = 94.20%). (h) miniGCN (OA = 84.59%). (i) SpectralFormer (OA = 95.73%). (j) SpectralDiff (OA = 98.82%).

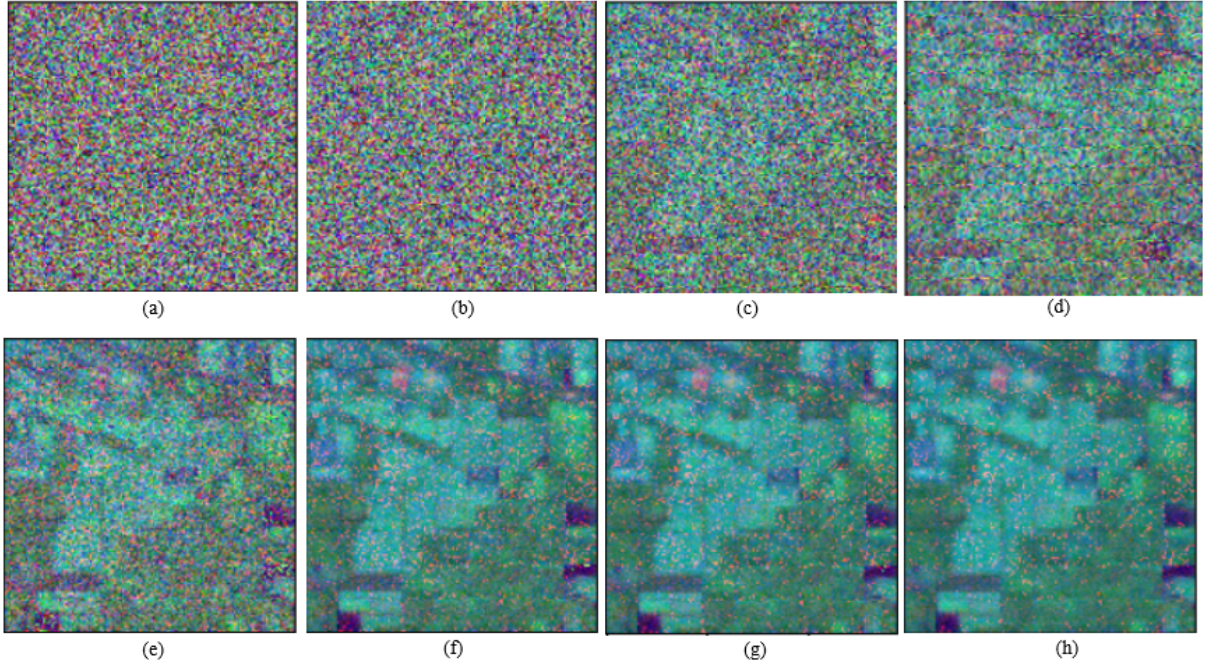


Fig. 9: False-color images of the reconstructed IndianPines dataset corresponding to different timestamps by Reverse Spectral-Spatial Diffusion Process. (a)  $t = 400$ . (b)  $t = 200$ . (c)  $t = 100$ . (d)  $t = 80$ . (e)  $t = 50$ . (f)  $t = 10$ . (g)  $t = 5$ . (h)  $t = 0$ .

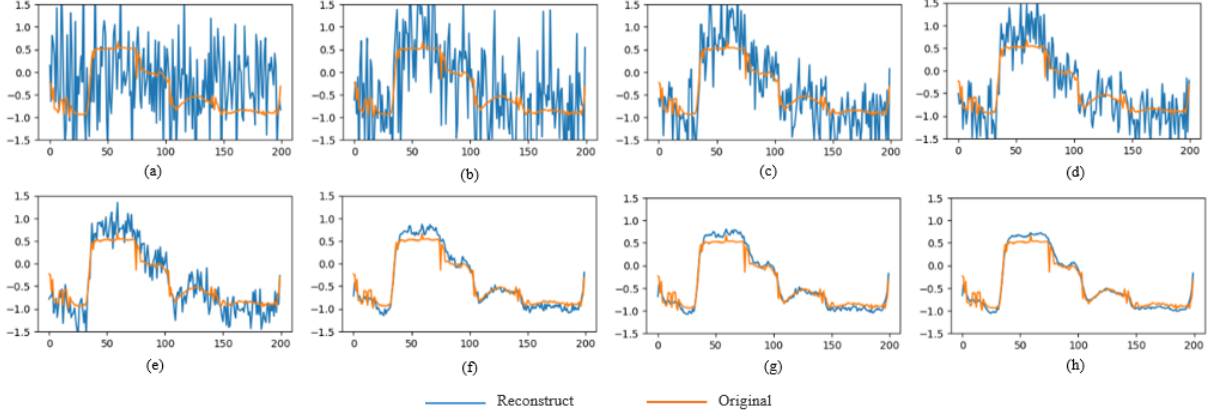


Fig. 10: The spectral curves of the reconstructed Indian Pines dataset corresponding to different timestamps by Reverse Spectral-Spatial Diffusion Process, class=woods, x-axis:spectral band number, y-axis: normalized spectral values. (a)  $t = 400$ . (b)  $t = 200$ . (c)  $t = 100$ . (d)  $t = 80$ . (e)  $t = 50$ . (f)  $t = 10$ . (g)  $t = 5$ . (h)  $t = 0$ .

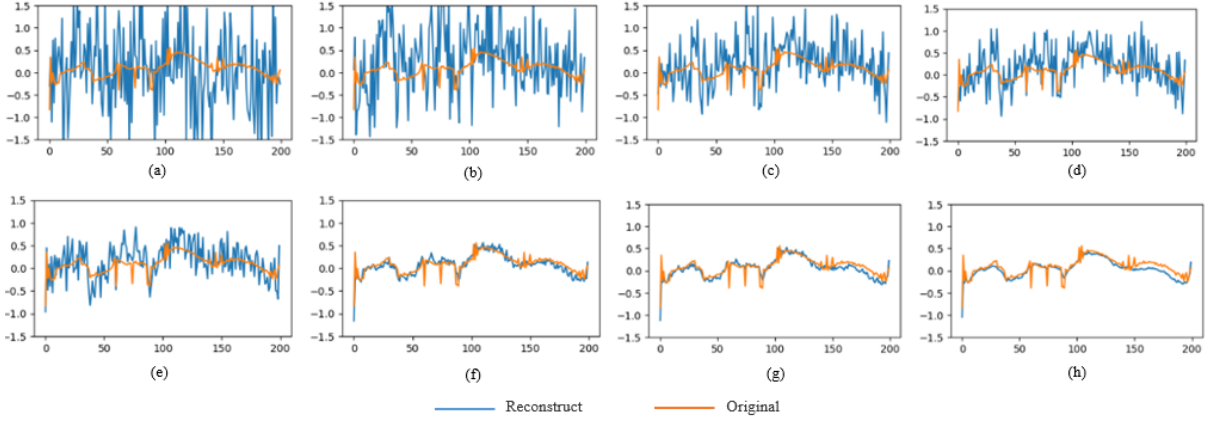


Fig. 11: The spectral curves of the reconstructed Indian Pines dataset corresponding to different timestamps by Reverse Spectral-Spatial Diffusion Process, class=SoybeanMintill, x-axis: spectral band number, y-axis: normalized spectral values. (a)  $t = 400$ . (b)  $t = 200$ . (c)  $t = 100$ . (d)  $t = 80$ . (e)  $t = 50$ . (f)  $t = 10$ . (g)  $t = 5$ . (h)  $t = 0$ .

TABLE V  
CLASSIFICATION PERFORMANCE ANALYSIS BETWEEN  
DIFFERENT FEATURE INPUT ON THE INDIAN PINES  
DATASET, PAVIA UNIVERSITY DATASET AND HOUSTON  
2013 DATASET

Dataset	Model	Feature Input	Metrics		
			OA(%)	AA(%)	$\kappa$ *100
IP	Transformer	Raw Feature	95.37	89.26	94.72
		Diffusion	98.34	93.33	98.11
PU		Raw Feature	98.55	97.66	98.07
		Diffusion	99.48	98.96	99.30
HU		Raw Feature	96.31	96.65	96.01
			Diffusion	98.82	98.55

ple, Fig. 9 presents the restoration effects corresponding to different timestamps on the Indian Pines dataset using a false-color image. From a visual perspective, the diffusion model basically reconstructs the original remote sensing image

content. Additionally, Figs. 10-11 show the restoration process for two different spectral curves of land-cover types. As the timestamps change, the spectral curves gradually reconstruct to the original shape of the land-cover types from a state similar to white noise. This indicates that the diffusion model has embedded the spectral curve information into the model parameters, providing a data foundation for using the diffusion feature for land-cover classification.

When extracting features using the Diffusion model, there are two crucial influencing parameters to consider, namely the timestamp and the layerindex. Timestamp refers to the number of denoising steps the Diffusion model takes to restore noisy images additionally. Layerindex refers to the location of the U-Net output used as a feature layer in the Diffusion model. We have conducted classification experiments on various timestamp and layerindex values, and the results are presented in the Table VI. In the case of the Indian Pines dataset, there are some fluctuations in classification performance for different timestamp and layer index values, but no significant changes. However, for the Pavia University and Houston 2013 datasets, there

TABLE VI  
THE PERFORMANCE OF DIFFERENT LAYERINDEX AND TIMESTAMP IN THE INDIAN PINES DATASET, THE PAVIA UNIVERSITY DATASET, AND THE HOUSTON 2013 DATASET

LayerIndex	Timestamp	Indian Pines			Pavia University			Houston 2013		
		OA(%)	AA(%)	$\kappa * 100$	OA(%)	AA(%)	$\kappa * 100$	OA(%)	AA(%)	$\kappa * 100$
0	5	98.02	91.73	97.74	99.31	98.51	99.08	98.61	98.42	98.50
	10	98.09	90.66	97.83	99.15	98.05	98.87	98.62	98.46	98.51
	100	97.91	89.15	97.62	99.04	97.87	98.72	97.57	97.49	97.37
	200	97.84	91.52	97.54	97.78	95.71	97.04	96.23	96.26	95.92
1	5	98.34	93.33	98.11	99.39	98.84	99.19	98.82	98.55	98.73
	10	97.93	90.02	97.64	99.48	98.96	99.30	98.72	98.42	98.62
	100	98.03	92.55	97.75	98.70	97.73	98.27	97.85	97.78	97.67
	200	97.99	93.49	97.71	97.82	96.16	97.11	96.30	96.45	96.00
2	5	98.18	92.10	97.92	99.01	98.39	98.68	97.83	97.74	97.66
	10	97.90	91.63	97.60	99.11	98.57	98.82	97.55	97.23	97.35
	100	98.16	91.37	97.90	96.99	94.49	95.99	94.63	94.73	94.19
	200	98.21	92.27	97.96	94.98	91.11	93.31	92.77	93.15	92.18

1 LayerIndex=0, 1, 2 respectively represent the inputs of the three up-sampling layers in the U-Net model, with larger numbers closer to the output layer.  
2 A smaller Timestamp indicates that the diffusion denoising process is closer to the original image position.

is a certain correlation between classification performance and timestamp/layerindex. When considering the timestamp dimension, a decreasing trend in classification performance is observed when using features with larger timestamps (such as timestamp=100, 200), and the optimal performance generally occurs in smaller timestamp groups (such as timestamp = 5, 10). We believe that when the timestamp is larger, the number of iterations for denoising using the Diffusion model is lower, leading to relatively more noise information in the input and resulting in a deviation in the classification performance. Considering the layer index dimension, both datasets showed better performance at layerindex=0,1 than at layerindex=2.

## V. CONCLUSION

In this paper, a novel approach for constructing the relationship between hyperspectral samples with spectral-spatial diffusion process is proposed. The proposed approach provides a unique perspective on the spectral-spatial diffusion process, which plays a critical role in establishing the global relationship between samples. By extracting spectral-spatial diffusion features, cross sample perception can be achieved. A plethora of empirical evidence has demonstrated the superiority of the proposed methodology over existing state-of-the-art techniques.

As we turn towards the future, a promising avenue of exploration lies in the investigation of novel global modeling methodologies, hinging on generative paradigms. By harnessing such techniques, we stand to realize the potential for seamless, end-to-end cross-sample relationship mining and HSI classification, thereby enabling a more nuanced and comprehensive understanding of complex HSI datasets.

## REFERENCES

- [1] S. Li, W. Song, L. Fang, Y. Chen, P. Ghamisi, and J. A. Benediktsson, "Deep learning for hyperspectral image classification: An overview," *IEEE Transactions on Geoscience and Remote Sensing*, vol. 57, no. 9, pp. 6690–6709, 2019.
- [2] L. Zhang, L. Zhang, and B. Du, "Deep learning for remote sensing data: A technical tutorial on the state of the art," *IEEE Geoscience and Remote Sensing Magazine*, vol. 4, no. 2, pp. 22–40, 2016.
- [3] X. X. Zhu, D. Tuia, L. Mou, G.-S. Xia, L. Zhang, F. Xu, and F. Fraundorfer, "Deep learning in remote sensing: A comprehensive review and list of resources," *IEEE Geoscience and Remote Sensing Magazine*, vol. 5, no. 4, pp. 8–36, 2017.
- [4] P. Ghamisi, J. Plaza, Y. Chen, J. Li, and A. J. Plaza, "Advanced spectral classifiers for hyperspectral images: A review," *IEEE Geoscience and Remote Sensing Magazine*, vol. 5, no. 1, pp. 8–32, 2017.
- [5] S. Prasad and L. M. Bruce, "Limitations of principal components analysis for hyperspectral target recognition," *IEEE Geoscience and Remote Sensing Letters*, vol. 5, no. 4, pp. 625–629, 2008.
- [6] J. Harris, D. Rogge, R. Hitchcock, O. Jewliw, and D. Wright, "Mapping lithology in canada's arctic: application of hyperspectral data using the minimum noise fraction transformation and matched filtering," *Canadian Journal of Earth Sciences*, vol. 42, no. 12, pp. 2173–2193, 2005.
- [7] Y. W. Chen and X. H. Han, *Classification of High-Resolution Satellite Images Using Supervised Locality Preserving Projections*. Springer Berlin Heidelberg, 2008.
- [8] Q. Du and H. Ren, "Real-time constrained linear discriminant analysis to target detection and classification in hyperspectral imagery," *Pattern Recognition*, vol. 36, no. 1, pp. 1–12, 2003.
- [9] J. Wang and C.-I. Chang, "Independent component analysis-based dimensionality reduction with applications in hyperspectral image analysis," *IEEE Transactions on Geoscience and Remote Sensing*, vol. 44, no. 6, pp. 1586–1600, 2006.
- [10] L. Xie, M. Yin, X. Yin, Y. Liu, and G. Yin, "Low-rank sparse preserving projections for dimensionality reduction," *IEEE Transactions on Image Processing*, vol. 27, no. 11, pp. 5261–5274, 2018.
- [11] A. Plaza, P. Martinez, J. Plaza, and R. Perez, "Dimensionality reduction and classification of hyperspectral image data using sequences of extended morphological transformations," *IEEE Transactions on Geoscience & Remote Sensing*, vol. 43, no. 3, pp. 466–479, 2005.
- [12] P. R. Marpu, M. Pedernana, M. D. Mura, J. A. Benediktsson, and L. Bruzzone, "Automatic generation of standard deviation attribute profiles for spectral-spatial classification of remote sensing data," *IEEE Geoscience & Remote Sensing Letters*, vol. 10, no. 2, pp. 293–297, 2013.
- [13] G. E. Hinton and R. R. Salakhutdinov, "Reducing the dimensionality of data with neural networks," *science*, vol. 313, no. 5786, pp. 504–507, 2006.
- [14] J. Yue, L. Fang, P. Ghamisi, W. Xie, J. Li, J. Chanussot, and A. J. Plaza, "Optical remote sensing image understanding with weak supervision: Concepts, methods, and perspectives," *IEEE Geoscience and Remote Sensing Magazine*, pp. 2–21, 2022.
- [15] K. He, X. Zhang, S. Ren, and J. Sun, "Deep residual learning for image recognition," in *2016 IEEE Conference on Computer Vision and Pattern Recognition (CVPR)*, 2016, pp. 770–778.

- [16] S. Wang, J. Yue, J. Liu, Q. Tian, and M. Wang, "Large-scale few-shot learning via multi-modal knowledge discovery," in *European Conference on Computer Vision*. Springer, 2020, pp. 718–734.
- [17] L. Chen, G. Papandreou, I. Kokkinos, K. Murphy, and A. L. Yuille, "DeepLab: Semantic image segmentation with deep convolutional nets, atrous convolution, and fully connected crfs," *IEEE Transactions on Pattern Analysis and Machine Intelligence*, vol. 40, no. 4, pp. 834–848, 2018.
- [18] Z. Tian, H. Zhao, M. Shu, Z. Yang, R. Li, and J. Jia, "Prior guided feature enrichment network for few-shot segmentation," *IEEE Transactions on Pattern Analysis and Machine Intelligence*, pp. 1–1, 2020.
- [19] L. Fang, Y. Jiang, Y. Yan, J. Yue, and Y. Deng, "Hyperspectral image instance segmentation using spectral-spatial feature pyramid network," *IEEE Transactions on Geoscience and Remote Sensing*, vol. 61, pp. 1–13, 2023.
- [20] R. Girshick, J. Donahue, T. Darrell, and J. Malik, "Region-based convolutional networks for accurate object detection and segmentation," *IEEE Transactions on Pattern Analysis and Machine Intelligence*, vol. 38, no. 1, pp. 142–158, 2016.
- [21] S. Ren, K. He, R. Girshick, and J. Sun, "Faster r-cnn: Towards real-time object detection with region proposal networks," *IEEE Transactions on Pattern Analysis and Machine Intelligence*, vol. 39, no. 6, pp. 1137–1149, 2017.
- [22] L. Fang, D. Zhu, J. Yue, B. Zhang, and M. He, "Geometric-spectral reconstruction learning for multi-source open-set classification with hyperspectral and lidar data," *IEEE/CAA Journal of Automatica Sinica*, vol. 9, no. 10, pp. 1892–1895, 2022.
- [23] J. Yue, D. Zhu, L. Fang, P. Ghamisi, and Y. Wang, "Adaptive spatial pyramid constraint for hyperspectral image classification with limited training samples," *IEEE Transactions on Geoscience and Remote Sensing*, pp. 1–14, 2021.
- [24] Y. Chen, Z. Lin, X. Zhao, G. Wang, and Y. Gu, "Deep learning-based classification of hyperspectral data," *IEEE Journal of Selected topics in Applied Earth Observations and Remote Sensing*, vol. 7, no. 6, pp. 2094–2107, 2014.
- [25] C. Zhang, J. Yue, and Q. Qin, "Global prototypical network for few-shot hyperspectral image classification," *IEEE Journal of Selected Topics in Applied Earth Observations and Remote Sensing*, pp. 1–1, 2020.
- [26] J. Yue, S. Mao, and M. Li, "A deep learning framework for hyperspectral image classification using spatial pyramid pooling," *Remote Sensing Letters*, vol. 7, no. 9, pp. 875–884, 2016.
- [27] D. Hong, Z. Han, J. Yao, L. Gao, B. Zhang, A. Plaza, and J. Chanussot, "Spectralformer: Rethinking hyperspectral image classification with transformers," *IEEE Transactions on Geoscience and Remote Sensing*, vol. 60, pp. 1–15, 2022.
- [28] X. Cao, Y. Ge, R. Li, J. Zhao, and L. Jiao, "Hyperspectral imagery classification with deep metric learning," *Neurocomputing*, vol. 356, pp. 217–227, 2019.
- [29] A. Qin, Z. Shang, J. Tian, Y. Wang, T. Zhang, and Y. Y. Tang, "Spectral-spatial graph convolutional networks for semisupervised hyperspectral image classification," *IEEE Geoscience and Remote Sensing Letters*, vol. 16, no. 2, pp. 241–245, 2019.
- [30] S. Wan, C. Gong, P. Zhong, S. Pan, G. Li, and J. Yang, "Hyperspectral image classification with context-aware dynamic graph convolutional network," *IEEE Transactions on Geoscience and Remote Sensing*, vol. 59, no. 1, pp. 597–612, 2021.
- [31] D. Hong, L. Gao, J. Yao, B. Zhang, A. Plaza, and J. Chanussot, "Graph convolutional networks for hyperspectral image classification," *IEEE Transactions on Geoscience and Remote Sensing*, vol. 59, no. 7, pp. 5966–5978, 2021.
- [32] J. A. Benediktsson and P. Ghamisi, *Spectral-spatial classification of hyperspectral remote sensing images*. Artech House, 2015.
- [33] S. Liu, Q. Shi, and L. Zhang, "Few-shot hyperspectral image classification with unknown classes using multitask deep learning," *IEEE Transactions on Geoscience and Remote Sensing*, pp. 1–18, 2020.
- [34] J. Yue, L. Fang, H. Rahmani, and P. Ghamisi, "Self-supervised learning with adaptive distillation for hyperspectral image classification," *IEEE Transactions on Geoscience and Remote Sensing*, pp. 1–13, 2021.
- [35] J. Yue, L. Fang, and M. He, "Spectral-spatial latent reconstruction for open-set hyperspectral image classification," *IEEE Transactions on Image Processing*, vol. 31, pp. 5227–5241, 2022.
- [36] B. Rasti, D. Hong, R. Hang, P. Ghamisi, X. Kang, J. Chanussot, and J. A. Benediktsson, "Feature extraction for hyperspectral imagery: The evolution from shallow to deep (overview and toolbox)," *IEEE Geoscience and Remote Sensing Magazine*, 2020.
- [37] W. Li, S. Prasad, J. E. Fowler, and L. M. Bruce, "Locality-preserving discriminant analysis in kernel-induced feature spaces for hyperspectral image classification," *IEEE Geoscience & Remote Sensing Letters*, vol. 8, no. 5, pp. 894–898, 2011.
- [38] B. Raducanu and F. Dornaika, "A supervised non-linear dimensionality reduction approach for manifold learning," *Pattern Recognition*, vol. 45, no. 6, pp. 2432–2444, 2012.
- [39] Qiao, Lishan, Chen, Songcan, Tan, and Xiaoyang, "Sparsity preserving projections with applications to face recognition," *Pattern Recognition*, vol. 43, no. 1, pp. 331–341, 2010.
- [40] C. M. Bachmann, T. L. Ainsworth, and R. A. Fusina, "Improved manifold coordinate representations of large-scale hyperspectral scenes," *IEEE Transactions on Geoscience and Remote Sensing*, vol. 44, no. 10, pp. 2786–2803, 2006.
- [41] F. Tsai and J.-S. Lai, "Feature extraction of hyperspectral image cubes using three-dimensional gray-level cooccurrence," *IEEE Transactions on Geoscience and Remote Sensing*, vol. 51, no. 6, pp. 3504–3513, 2013.
- [42] L. Shen, Z. Zhu, S. Jia, J. Zhu, and Y. Sun, "Discriminative gabor feature selection for hyperspectral image classification," *IEEE Geoscience and Remote Sensing Letters*, vol. 10, no. 1, pp. 29–33, 2013.
- [43] Y. Zhou, J. Peng, and C. L. P. Chen, "Dimension reduction using spatial and spectral regularized local discriminant embedding for hyperspectral image classification," *IEEE Transactions on Geoscience and Remote Sensing*, vol. 53, no. 2, pp. 1082–1095, 2015.
- [44] D. Hong, N. Yokoya, J. Chanussot, J. Xu, and X. X. Zhu, "Joint and progressive subspace analysis (jpsa) with spatial-spectral manifold alignment for semisupervised hyperspectral dimensionality reduction," *IEEE Transactions on Cybernetics*, vol. 51, no. 7, pp. 3602–3615, 2021.
- [45] A. Kianisarkaleh and H. Ghassemian, "Spatial-spectral locality preserving projection for hyperspectral image classification with limited training samples," *International journal of remote sensing*, vol. 37, no. 21, pp. 5045–5059, 2016.
- [46] J. Yue, W. Zhao, S. Mao, and H. Liu, "Spectral-spatial classification of hyperspectral images using deep convolutional neural networks," *Remote Sensing Letters*, vol. 6, no. 6, pp. 468–477, 2015.
- [47] L. Mou, P. Ghamisi, and X. X. Zhu, "Deep recurrent neural networks for hyperspectral image classification," *IEEE Transactions on Geoscience and Remote Sensing*, vol. 55, no. 7, pp. 3639–3655, 2017.
- [48] Z. Zhong, J. Li, Z. Luo, and M. Chapman, "Spectral-spatial residual network for hyperspectral image classification: A 3-d deep learning framework," *IEEE Transactions on Geoscience and Remote Sensing*, vol. 56, no. 2, pp. 847–858, 2018.
- [49] M. E. Paoletti, J. M. Haut, R. Fernandez-Beltran, J. Plaza, A. J. Plaza, and F. Pla, "Deep pyramidal residual networks for spectral-spatial hyperspectral image classification," *IEEE Transactions on Geoscience and Remote Sensing*, vol. 57, no. 2, pp. 740–754, 2019.
- [50] M. E. Paoletti, J. M. Haut, R. Fernandez-Beltran, J. Plaza, A. Plaza, J. Li, and F. Pla, "Capsule networks for hyperspectral image classification," *IEEE Transactions on Geoscience and Remote Sensing*, vol. 57, no. 4, pp. 2145–2160, 2019.
- [51] A. Q. Nichol and P. Dhariwal, "Improved denoising diffusion probabilistic models," in *International Conference on Machine Learning*. PMLR, 2021, pp. 8162–8171.
- [52] D. Kingma, T. Salimans, B. Poole, and J. Ho, "Variational diffusion models," *Advances in neural information processing systems*, vol. 34, pp. 21 696–21 707, 2021.
- [53] J. Sohl-Dickstein, E. Weiss, N. Maheswaranathan, and S. Ganguli, "Deep unsupervised learning using nonequilibrium thermodynamics," in *International Conference on Machine Learning*. PMLR, 2015, pp. 2256–2265.
- [54] F.-A. Croitoru, V. Hondru, R. T. Ionescu, and M. Shah, "Diffusion models in vision: A survey," *arXiv preprint arXiv:2209.04747*, 2022.
- [55] J. Austin, D. D. Johnson, J. Ho, D. Tarlow, and R. van den Berg, "Structured denoising diffusion models in discrete state-spaces," *Advances in Neural Information Processing Systems*, vol. 34, pp. 17 981–17 993, 2021.
- [56] X. L. Li, J. Thickstun, I. Gulrajani, P. Liang, and T. B. Hashimoto, "Diffusion-lm improves controllable text generation," *arXiv preprint arXiv:2205.14217*, 2022.
- [57] J. M. L. Alcaraz and N. Strodthoff, "Diffusion-based time series imputation and forecasting with structured state space models," *arXiv preprint arXiv:2208.09399*, 2022.
- [58] K. Rasul, C. Seward, I. Schuster, and R. Vollgraf, "Autoregressive denoising diffusion models for multivariate probabilistic time series forecasting," in *International Conference on Machine Learning*. PMLR, 2021, pp. 8857–8868.
- [59] E. Hoogeboom, V. G. Satorras, C. Vignac, and M. Welling, "Equivariant diffusion for molecule generation in 3d," in *International Conference on Machine Learning*. PMLR, 2022, pp. 8867–8887.

- [60] B. Jing, G. Corso, J. Chang, R. Barzilay, and T. Jaakkola, "Torsional diffusion for molecular conformer generation," *arXiv preprint arXiv:2206.01729*, 2022.
- [61] L. Yang, Z. Zhang, Y. Song, S. Hong, R. Xu, Y. Zhao, Y. Shao, W. Zhang, B. Cui, and M.-H. Yang, "Diffusion models: A comprehensive survey of methods and applications," *arXiv preprint arXiv:2209.00796*, 2022.
- [62] Y. Song and S. Ermon, "Generative modeling by estimating gradients of the data distribution," *Advances in neural information processing systems*, vol. 32, 2019.
- [63] A. Vahdat, K. Kreis, and J. Kautz, "Score-based generative modeling in latent space," in *Advances in Neural Information Processing Systems*, M. Ranzato, A. Beygelzimer, Y. Dauphin, P. Liang, and J. W. Vaughan, Eds., vol. 34. Curran Associates, Inc., 2021, pp. 11 287–11 302.
- [64] Y. Song and S. Ermon, "Improved techniques for training score-based generative models," in *Advances in Neural Information Processing Systems*, H. Larochelle, M. Ranzato, R. Hadsell, M. Balcan, and H. Lin, Eds., vol. 33. Curran Associates, Inc., 2020, pp. 12 438–12 448.
- [65] Y. Song, C. Durkan, I. Murray, and S. Ermon, "Maximum likelihood training of score-based diffusion models," *Advances in Neural Information Processing Systems*, vol. 34, pp. 1415–1428, 2021.
- [66] Y. Song, J. Sohl-Dickstein, D. P. Kingma, A. Kumar, S. Ermon, and B. Poole, "Score-based generative modeling through stochastic differential equations," in *International Conference on Learning Representations*, 2020.
- [67] J. Ho, A. Jain, and P. Abbeel, "Denoising diffusion probabilistic models," in *Advances in Neural Information Processing Systems*, H. Larochelle, M. Ranzato, R. Hadsell, M. Balcan, and H. Lin, Eds., vol. 33. Curran Associates, Inc., 2020, pp. 6840–6851.
- [68] P. Dhariwal and A. Nichol, "Diffusion models beat gans on image synthesis," *Advances in Neural Information Processing Systems*, vol. 34, pp. 8780–8794, 2021.
- [69] J. Yue, L. Fang, S. Xia, Y. Deng, and J. Ma, "Dif-fusion: Towards high color fidelity in infrared and visible image fusion with diffusion models," *arXiv preprint arXiv:2301.08072*, 2023.
- [70] A. Lugmayr, M. Danelljan, A. Romero, F. Yu, R. Timofte, and L. Van Gool, "Repaint: Inpainting using denoising diffusion probabilistic models," in *Proceedings of the IEEE/CVF Conference on Computer Vision and Pattern Recognition (CVPR)*, 2022, pp. 11 461–11 471.
- [71] C. Saharia, W. Chan, H. Chang, C. Lee, J. Ho, T. Salimans, D. Fleet, and M. Norouzi, "Palette: Image-to-image diffusion models," in *ACM SIGGRAPH 2022 Conference Proceedings*, 2022, pp. 1–10.
- [72] M. Zhao, F. Bao, C. Li, and J. Zhu, "EGSDE: Unpaired image-to-image translation via energy-guided stochastic differential equations," in *Advances in Neural Information Processing Systems*, A. H. Oh, A. Agarwal, D. Belgrave, and K. Cho, Eds., 2022.
- [73] J. Wolleb, R. Sandkühler, F. Bieder, and P. C. Cattin, "The swiss army knife for image-to-image translation: Multi-task diffusion models," *arXiv preprint arXiv:2204.02641*, 2022.
- [74] C. Saharia, J. Ho, W. Chan, T. Salimans, D. J. Fleet, and M. Norouzi, "Image super-resolution via iterative refinement," *IEEE Transactions on Pattern Analysis and Machine Intelligence*, pp. 1–14, 2022.
- [75] M. Daniels, T. Maunu, and P. Hand, "Score-based generative neural networks for large-scale optimal transport," *Advances in neural information processing systems*, vol. 34, pp. 12 955–12 965, 2021.
- [76] H. Chung, B. Sim, and J. C. Ye, "Come-closer-diffuse-faster: Accelerating conditional diffusion models for inverse problems through stochastic contraction," in *Proceedings of the IEEE/CVF Conference on Computer Vision and Pattern Recognition (CVPR)*, 2022, pp. 12 413–12 422.
- [77] R. S. Zimmermann, L. Schott, Y. Song, B. A. Dunn, and D. A. Klindt, "Score-based generative classifiers," *arXiv preprint arXiv:2110.00473*, 2021.
- [78] S. Chen, P. Sun, Y. Song, and P. Luo, "Diffusiondet: Diffusion model for object detection," *arXiv preprint arXiv:2211.09788*, 2022.
- [79] D. Baranchuk, A. Voynov, I. Rubachev, V. Khurlov, and A. Babenko, "Label-efficient semantic segmentation with diffusion models," in *International Conference on Learning Representations*, 2021, pp. 1–15.
- [80] T. Amit, E. Nachmani, T. Shaharbany, and L. Wolf, "Segdiff: Image segmentation with diffusion probabilistic models," *arXiv preprint arXiv:2112.00390*, 2022.
- [81] S. Gu, D. Chen, J. Bao, F. Wen, B. Zhang, D. Chen, L. Yuan, and B. Guo, "Vector quantized diffusion model for text-to-image synthesis," in *Proceedings of the IEEE/CVF Conference on Computer Vision and Pattern Recognition (CVPR)*, June 2022, pp. 10 696–10 706.
- [82] W. Gedara Chaminda Bandara, N. Gopalakrishnan Nair, and V. M. Patel, "Remote sensing change detection (segmentation) using denoising diffusion probabilistic models," *arXiv e-prints*, pp. arXiv–2206, 2022.
- [83] W. Zhao and S. Du, "Spectral-spatial feature extraction for hyperspectral image classification: A dimension reduction and deep learning approach," *IEEE Transactions on Geoscience and Remote Sensing*, vol. 54, no. 8, pp. 4544–4554, 2016.
- [84] Y. Chen, H. Jiang, C. Li, X. Jia, and P. Ghamisi, "Deep feature extraction and classification of hyperspectral images based on convolutional neural networks," *IEEE Transactions on Geoscience and Remote Sensing*, vol. 54, no. 10, pp. 6232–6251, 2016.



**Ning Chen** received the B.S. degree from the School of Earth and Space Sciences, Peking University, Beijing, China, in 2016, and the M.S. degree in GIS from the School of Earth and Space Sciences, Peking University, Beijing, China in 2019.

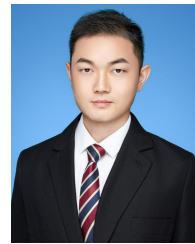
He is currently an Assistant Engineer with the Institute of Remote Sensing and Geographic Information System, Peking University. His research interests include satellite image understanding, recommendation system, large-scale sparse learning and pattern recognition.



**Jun Yue** received the B.Eng. degree in geodesy from Wuhan University, Wuhan, China, in 2013 and the Ph.D. degree in GIS from Peking University, Beijing, China, in 2018.

He is currently an Assistant Professor with the School of Automation, Central South University. His research interests include satellite image understanding, pattern recognition, and few-shot learning. Dr. Yue serves as a reviewer for IEEE Transactions on Image Processing, IEEE Transactions on Neural Networks and Learning Systems, IEEE Transactions

on Geoscience and Remote Sensing, ISPRS Journal of Photogrammetry and Remote Sensing, IEEE Geoscience and Remote Sensing Letters, IEEE Transactions on Biomedical Engineering, Information Fusion, Information Sciences, etc.



**Leyuan Fang** (Senior Member, IEEE) received the Ph.D. degree from the College of Electrical and Information Engineering, Hunan University, Changsha, China, in 2015.

From August 2016 to September 2017, he was a Postdoc Researcher with the Department of Biomedical Engineering, Duke University, Durham, NC, USA. He is currently a Professor with the College of Electrical and Information Engineering, Hunan University. His research interests include sparse representation and multi-resolution analysis in remote sensing and medical image processing. He is the associate editors of IEEE Transactions on Image Processing, IEEE Transactions on Geoscience and Remote Sensing, IEEE Transactions on Neural Networks and Learning Systems, and Neurocomputing. He was a recipient of one 2nd-Grade National Award at the Nature and Science Progress of China in 2019.



**Shaobo Xia** received the bachelor's degree in geodesy and geomatics from the School of Geodesy and Geomatics, Wuhan University, Wuhan, China, in 2013, the master's degree in cartography and geographic information systems from the Institute of Remote Sensing and Digital Earth, Chinese Academy of Sciences, Beijing, China, in 2016, and the Ph.D. degree in geomatics from the University of Calgary, Calgary, AB, Canada, in 2020.

He is an Assistant Professor with the Department of Geomatics Engineering, Changsha University of Science and Technology, Changsha, China. His research interests include point cloud processing and remote sensing.